



# Synthesis of Nanoscale ZSM-5 Zeolites for the Catalytic Cracking of Oleic Acid into Light Olefins and Aromatics

Hao Liu<sup>1</sup> · Yanlin Wang<sup>1</sup> · Hong Yuan<sup>1,2,3</sup> · Wenbo Luo<sup>1</sup>

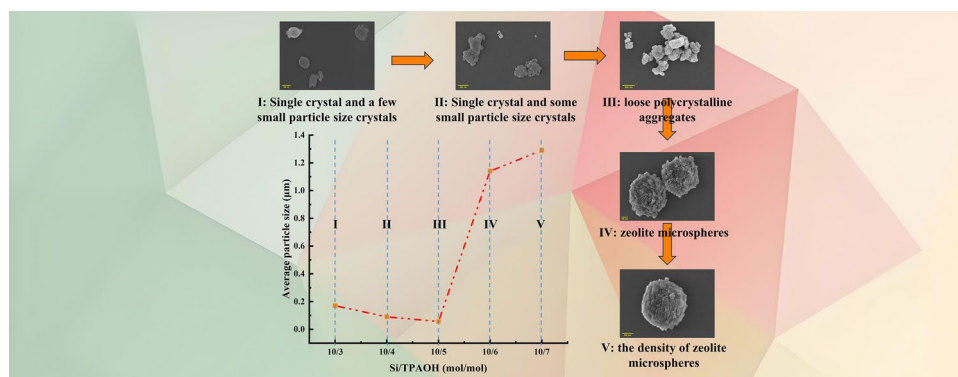
Received: 14 July 2024 / Accepted: 8 September 2024

© The Author(s), under exclusive licence to Springer Science+Business Media, LLC, part of Springer Nature 2024

## Abstract

Nanoscale ZSM-5 zeolites (NZSM-5) having different crystal sizes and Si/tetrapropylammonium hydroxide (TPAOH) molar ratios were synthesized using a hydrothermal method. These materials were characterized by X-ray diffraction, scanning electron microscopy, transmission electron microscopy, and N<sub>2</sub> adsorption–desorption. The results showed that each zeolite was highly crystalline regardless of the Si/TPAOH ratio and that the Brunauer–Emmett–Teller surface areas were in the range of 329–392 m<sup>2</sup>/g. The random aggregation of these nanoparticles resulted in the formation of numerous intergranular mesopores. These NZSM-5 zeolites were applied to the catalytic cracking of oleic acid to prepare light olefins and light aromatics using a laboratory-scale fixed bed reactor. The zeolite having a Si/TPAOH ratio of 10/5 showed the best catalytic activity and provided light olefins yield of 55% and selectivity of BTX in liquid phase products of 18%, respectively, at 500 °C. The small crystal size and abundant intergranular mesopores in this specimen resulted in shorter diffusion paths and an increase in the external specific surface area that both inhibited coke deposition and ensured accessible acid sites.

## Graphical Abstract



**Keywords** Nanoscale ZSM-5 zeolite · Light olefin · Intergranular mesoporous · Crystal sizes · BTX

✉ Hong Yuan  
yuanhong@nun.edu.cn

Hao Liu  
643368063@qq.com

Yanlin Wang  
2962794253@qq.com

Wenbo Luo  
444281833@qq.com

<sup>1</sup> School of Chemistry and Chemical Engineering, North Minzu University, Yinchuan 750021, China

<sup>2</sup> Key Laboratory for Chemical Engineering and Technology, State Ethnic Affairs Commission, North Minzu University, Yinchuan 750021, China

<sup>3</sup> Ningxia Key Laboratory of Solar Chemical Conversion Technology, North Minzu University, Yinchuan 750021, China

## 1 Introduction

Light olefins (comprising ethene, propene, and butenes; LOs) and light aromatics (comprising benzene, toluene, and xylenes; BTX) are important chemical raw materials that are widely used in the manufacture of pharmaceuticals, pesticides, dyes, polymers, and other substances [1, 2]. At present, LOs and BTX are primarily produced from petroleum [3] although in recent years the synthesis of LOs and BTX based on the catalytic cracking of biomass has received extensive attention [4, 5]. Animal fats, vegetable oils, and waste cooking oils tend to have high hydrogen/carbon ratios and low oxygen contents and so may be good raw materials for the production of LOs and BTX in this manner [6, 7]. In particular, the use of waste cooking oil represents an economical alternative.

Because of their special channel structures, ZSM-5 zeolites are widely used in the preparation of LOs and BTX. ZSM-5 zeolites possess three-dimensional channel network structures formed by a cross between elliptically cross-sectioned ( $5.3 \times 5.6 \text{ \AA}$ ) straight channels and approximately circularly cross-sectioned ( $5.1 \times 5.5 \text{ \AA}$ ) sinusoidal channels. In the case that greases are used as raw materials in conjunction with this zeolite, LOs are generated through cracking reactions while some olefins are cyclized and dehydrogenated to give BTX [8]. ZSM-5 zeolite also contains numerous Brønsted acid sites (B acid sites) and Lewis acid sites (L acid sites) that contribute to the generation of LOs and BTX. Specifically, long-chain alkanes in greases undergo cracking and dehydrogenation at the B acid sites to form olefins whereas olefins undergo Diels-Alder cyclization reactions at the L acid sites to generate cycloalkanes [9]. Finally, the cycloalkanes are converted to aromatic hydrocarbons by dehydrogenation-aromatization at the B acid sites [10]. Guan et al. [11] found that the cracking of long-chain alkanes to light alkenes using ZSM-5 required the participation of straight channels, which promote carbenium ion generation. Huang et al. [12] found that for monocyclic aromatic hydrocarbons (benzene and *ortho*- and *meta*-xylenes), the activation energy was much higher for diffusion through sinusoidal channels than through straight channels. In addition, the sinusoidal channel's size and ZSM-5's tortuous shape produced good aromatic selectivity. Even so, standard ZSM-5 zeolite has a structure based largely on micropores and the particle size of this zeolite is primarily on the micrometer scale. These characteristics can lead to carbon deposition caused by overreaction as well as the clogging of pores by such carbon. He et al. [13] used commercial ZSM-5 zeolite (Commer-Z-5) to catalytically crack oleic acid and produce LOs, and the total gas production and yield of LOs were 55 and 29 mL/g, respectively, at 400 °C. The authors found that Commer-Z-5 possessed numerous microporous

structures that were easily and rapidly coked, which reduced the catalytic activity. Yang et al. [14] hydrothermally prepared HZSM-5 and applied it to catalyze the transformation from glycerol to aromatics. At 400 °C, the BTX aromatic yield was 17.8%, and the catalyst's service lifetime was only 3 h because HZSM-5 is a typical microporous material containing large crystals. Because the reactants' diffusion path was long, glycerol was easily trapped in the catalyst during aromatization and subsequent methylation, forming heavy aromatics and, finally, rich carbon deposits on the zeolite surface, which deactivated the catalyst. Nano ZSM-5 zeolite provides significantly shorter diffusion paths, abundant intergranular mesopores, and accessible acid sites, thereby improving the catalytic activity of the material. Zhao et al. [15] hydrothermally synthesized a MZSM-5-B catalyst, possessing an average particle size of 69 nm, for catalytically cracking oleic acid to produce LOs. At 400 °C, the yield of LOs was as high as 111 mL/g because MZSM-5-B's rich mesoporous structure was conducive to rapid mass transfer, substantially improving both the catalyst's anti-coking ability and yield of LOs. Xu et al. [16] synthesized S-HZSM-5-0.75, a highly crystalline nano-zeolite possessing an average particle size of approximately 50 nm, by adding sodium alginate to a zeolite precursor solution, and used S-HZSM-5-0.75 to catalyze the transformation from glycerol to aromatics. At 400 °C, the BTX yield reached 35.06%, and the catalyst's service lifetime was 8.5 h. Konno et al. [17] used an emulsion to synthesize a ZSM-5 nano-zeolite, possessing 90-nm crystals, for cracking *n*-hexane to produce light alkenes. The effects of different temperatures (550, 600, and 650 °C) on the yield of LOs were investigated, and the highest yield of LOs (50.4%) was obtained at 650 °C, which was attributed to the rapid dehydrogenation at high temperatures. In addition, the effect of the ZSM-5 zeolite's crystal sizes (90 and 2300 nm) on the catalytic activity was also investigated, and the results showed that the catalytic activity and stability of the 90-nm ZSM-5 crystals were superior to those of the 2300 nm ZSM-5 crystals. Yi et al. [18] developed a catalyst by combining ZSM-5 nano-zeolite with CaO from organic calcium precursors (Org-CaO/NZSM-5) to catalyze the pyrolysis of de-oiled *Jatropha*-seed cakes. The results showed that the aromatic proportion was as high as 93% in the obtained bio-oil and that the combined BTX and naphthalene yield was approximately 70%, which was almost twice that obtained using conventional CaO/ZSM-5. Clearly, the synthesized nano-zeolite had a large specific surface area, numerous intergranular mesopores, and a short diffusion path, which are conducive to the diffusion of reactants and products and can effectively reduce carbon deposition on the zeolite surface. Therefore, in this work, smaller ZSM-5 zeolite nanoparticles were prepared and efficiently used to catalyze oleic acid cracking.

The size of ZSM-5 zeolite particles is largely determined by the balance between the rate of tetraethyl orthosilicate (TEOS) hydrolysis and the rate of crystal nucleation [19, 20]. This balance can be adjusted by varying the crystallization temperature, the proportion of water in the reaction mixture and the Si/Al ratio. Aguado et al. [21] synthesized nano-scale ZSM-5 formed by the aggregation of ultra-small nanocrystals (10–20 nm) at low temperatures. These reduced temperatures were found to favor the nucleation and crystallization of amorphous solid gels. Compared with the conventional ZSM-5 zeolite, this nano-scale ZSM-5 had a higher external surface area (202 m<sup>2</sup>/g) and a greater Brunauer-Emmett-Teller surface area (504 m<sup>2</sup>/g). These characteristics resulted in a significant increase in the number of catalytically active sites on the outside that promoted the catalytic cracking of macromolecules. However, the low temperature crystallization process also resulted in a low zeolite yield and required long crystallization times of 9 to 24 days. Su et al. [22] synthesized a nano ZSM-5 (AlZ5-D) using a dry-gel conversion method and obtained cylindrical aggregates based on the accumulation of ultrafine particles. The presence of abundant micropores and intergranular mesopores in the AlZ5-D facilitated the diffusion of bulky molecules to active sites on the catalyst. Although this synthesis method provided a high nucleation density it involved challenges related to slow crystal growth. Agarwal et al. [20] synthesized hierarchical nano-HZSM5 single crystals having different crystal sizes (30–40 nm) by varying the amount of water in the gel. Reducing the water content increased the Na<sup>+</sup> concentration, which in turn enhanced the nucleation effect, leading to the formation of smaller crystals. However, this synthesis method provided low zeolite yields. Wang et al. [23] found that reducing the SiO<sub>2</sub>/Al<sub>2</sub>O<sub>3</sub> ratio from 100 to 40 in the raw material mixture reduced the ZSM-5 particle size from 200 nm to approximately 50 nm. The same work showed that a high SiO<sub>2</sub>/Al<sub>2</sub>O<sub>3</sub> ratio promoted crystallization of the ZSM-5.

Other studies have demonstrated that increasing the template concentration reduces the zeolite particle size by enhancing dissolution of the silica source and increasing the rate of supersaturation. Karimi et al. [24] found that changing the Si/tetrapropylammonium hydroxide (TPAOH) molar ratio from 10/0.29 to 10/0.83 reduced the ZSM-5 zeolite grain size from 24.5 to 6.0 μm. Xu et al. [19] prepared TS-1 having different crystal sizes by varying the amounts of TPAOH used as a templating agent and reported that changing the Si/TPAOH molar ratio from 10/1 to 10/2 lowered the particle size from 900 to 200 nm. Increases in the amount of TPAOH would be expected to produce a more alkaline solution that would more readily dissolve Si species. However, some researchers have found that an excess of the templating agent can give overly large particles. As an example, Song et al. [25] synthesized intracrystalline mesoporous ZSM-5

using an organosiloxane as a mesopore-directing template. The particle size of this material was varied from 500 nm to 3 μm by changing the Si/TPAOH molar ratio from 10/12.5 to 10/22.5. An excess of TPAOH evidently results in rapid growth of the ZSM-5 framework and the formation of larger particles.

In fact, smaller zeolite crystals shorten the diffusion distance of the reactants and products and, therefore, the residence time in the zeolite, which, in turn, inhibits the overreaction producing heavy hydrocarbons and coke and stabilizes the catalyst [26]. However, the ZSM-5 nano-zeolites obtained by changing the contents of the template agents, such as TPAOH, failed to limit the crystal size below 200 nm. In this work, a NZSM-5 nano-zeolite possessing an average particle size of 56 nm was hydrothermally synthesized, and the effect of the Si/tetrapropylammonium hydroxide (TPAOH) molar ratio on the particle size was investigated. In addition, because the crystallization time substantially affects the zeolite's morphology and structure, the effects of the crystallization time in the range 0–216 h on the NZSM-5's crystallinity and morphology and crystal formation were investigated. Furthermore, the morphology, structural features and acidity of the NZSM-5 were systematically and comprehensively characterized. Finally, the effects of the NZSM-5 crystal size and of temperature on the reaction of oleic acid to produce LOs and BTX were studied in a laboratory-scale fixed bed reactor.

## 2 Experimental

### 2.1 Materials

Tetraethyl orthosilicate (TEOS, 98%), aluminum nitrate nonahydrate (Al(NO<sub>3</sub>)<sub>3</sub>·9H<sub>2</sub>O, 99%), aluminium isopropoxide (AIP, ≥98%), sodium hydroxide (NaOH, 96%), and oleic acid were purchased from Aladdin Biochemical Technology Co., Ltd. (China). Tetra propylammonium hydroxide (TPAOH, 25 wt%) were purchased from Innochem Technology Co., Ltd. (China).

### 2.2 Preparation of Catalysts

NZSM-5 was synthesized using a method previously reported by Mochizuki et al. [27] Briefly, 25.4 g of TEOS was combined with 60 g of deionized water and either 29.8, 39.7, 49.6, 59.5–69.4 g of TPAOH (in the form of a 25 wt% aqueous solution) to produce solution (A) In addition, 1.43 g of Al(NO<sub>3</sub>)<sub>3</sub>·9H<sub>2</sub>O and 0.49 g of NaOH were added to 27.78 g of deionized water with stirring to produce solution (B) The prepared solutions A and B were then combined and refluxed at 100 °C for 24 h to give a gel in which the molar ratios of the components were 1 SiO<sub>2</sub> : 0.015625

$\text{Al}_2\text{O}_3$ :0.3/0.4/0.5/0.6/0.7 TPAOH:0.05  $\text{Na}_2\text{O}$ :40  $\text{H}_2\text{O}$  (Si/Al ratio was 32). This gel was transferred to an autoclave reactor and maintained at 170 °C for 144 h. The solid product was then separated, dried at 120 °C for 12 h, and calcined at 550 °C for 5 h to obtain the NZSM-5 (Na-form). The NZSM-5 specimens with Si/TPAOH molar ratios of 10/3, 10/4, 10/5, 10/6, and 10/7 are referred to herein as NZSM-5-10/3, NZSM-5-10/4, NZSM-5-10/5, NZSM-5-10/6, and NZSM-5-10/7, respectively.

The gel which the molar ratios of the components were 1  $\text{SiO}_2$ :0.015625  $\text{Al}_2\text{O}_3$ :0.5TPAOH:0.05  $\text{Na}_2\text{O}$ :40  $\text{H}_2\text{O}$  (Si/Al ratio was 32) was transferred to an autoclave reactor and maintained at 170 °C for 0, 6, 7, 8, 9, 10, 11, 12, 24, 48, 72, 96, 120, 168, 192, and 216 h, respectively. The solid product was then separated, dried at 120 °C for 12 h, and calcined at 550 °C for 5 h to obtain the NZSM-5 (Na-form) with different crystallization times (0, 6, 7, 8, 9, 10, 11, 12, 24, 48, 72, 96, 120, 168, 192, and 216 h, respectively).

The conventional ZSM-5 (CZSM-5) was prepared based on a method reported by Wu et al. [28] In this process, 13.6 g of TPAOH and 20 g of deionized water were combined and stirred at 35 °C for 0.5 h, after which 0.62 g AIP and 1.0 g NaOH were added successively followed by further stirring until all reagents were completely dissolved. Following this, a 20.5 g quantity of TEOS was slowly added to the mixture with subsequent stirring for 16 h to obtain a gel having the molar ratios 1  $\text{SiO}_2$ :0.015625  $\text{Al}_2\text{O}_3$ :0.26 NaOH:0.17 TPAOH:11.3  $\text{H}_2\text{O}$ . (Si/Al ratio was 32) This gel was transferred to a hydrothermal reactor and held at 180 °C for 48 h. After centrifugation and washing, the solid product was dried at 100 °C for 10 h and calcined at 550 °C for 6 h to obtain the ZSM-5 zeolite (Na-form).

### 2.3 Characterization of Catalysts

X-ray diffraction (XRD) was carried out using a SmartLab SE (Rigaku, Japan) diffractometer operated at 40 kV and 30 mA with Cu  $\text{K}\alpha$  radiation. Fourier transform infrared (FTIR) spectroscopy measurements were performed by a FTIR-650 (Gangdong, China) spectrometer in the range of 2000–400  $\text{cm}^{-1}$ . For FT-IR measurements, powder samples were mixed with KBr (1:100) and pressed into tablets. Field emission scanning electron microscope (FE-SEM) images of samples were obtained on an GeminiSEM 300 (ZEISS, Germany) microscope operating at 2–5 kV and all samples were coated with a thin gold layer prior to imaging. The microtopography and lattice fringes of the samples were determined by JEM-F200 (JEOL, Japan) transmission electron microscopy (TEM). Samples were prepared by placing droplets of the ethanol-diluted sol onto the copper grid coated with holey carbon film. The specific surface area and pore size distribution of samples were determined on ASAP 2020 HD88 automatic specific surface area and

porosity analyzer (Micromeritics, USA) by nitrogen adsorption-desorption technique at the liquid nitrogen temperature of 77 K. The specific surface area was calculated by the BET equation, the specific surface area of micropores was calculated by t-plot method, and the average pore size was obtained from the maxima of the pore size distribution curve calculated by the Barrett–Joyner–Halenda method using the adsorption branch of the isotherm. The macropores structure (> 50 nm) was evaluated by the mercury injection porosimetry using the Micromeritics Autopore V 9620 instrument (Micromeritics, USA). Temperature-programmed desorption of ammonia ( $\text{NH}_3$ -TPD) profiles were recorded with an AutoChem II 2920 chemisorption apparatus (Micromeritics, USA). About 60 mg sample was pretreated at 500 °C with an Ar flow of 30 mL/min for 30 min, then cooled to 50 °C and adsorbed a mixture gas (10%  $\text{NH}_3$  and 90% He, 30 mL/min) for 60 min. Subsequently, the temperature was raised to 600 °C (10 °C/min) in He atmosphere (30 mL/min) and maintained for 60 min, in the meantime, the signal of desorbed  $\text{NH}_3$  was monitored by a thermal conductivity detector (TCD). The thermogravimetric (TG) analysis of the samples was performed on a thermal analyzer (HITACHI STA200, Japan) under Air atmosphere.  $^{27}\text{Al}$  MAS NMR spectra were performed using a AVANCE III 400 MHz spectrometer (Bruker, Germany). A selective  $\pi/12$  pulse was used for quantitative analysis of  $^{27}\text{Al}$  magic angle spinning (MAS) nuclear magnetic resonance (NMR) spectroscopy ( $^{27}\text{Al}$  MAS NMR spectra). Infra-red spectroscopy of pyridine adsorption (Py-IR) of samples were performed on an in-situ infrared spectrometer (Tensor-27, Bruker, Germany). The sample was pressed in the in-situ cell of the infrared spectrometer, sealed and vacuumed to  $10^{-3}$  Pa at 400 °C for 1 h to desorb the gas molecules on the surface of the sample and cooled to room temperature to collect the background value. Pyridine vapor was introduced into the in-situ cell and maintained for 30 min, then was heated to 150 °C and vacuumed to  $10^{-3}$  Pa again for 30 min. The sample was cooled to room temperature and scanned in the wavenumber range of 1400–1650  $\text{cm}^{-1}$ .

### 2.4 Catalytic Performance Tests

A laboratory-scale fixed bed apparatus was employed together with oleic acid as the raw material to investigate the performance of the catalyst. In each trial, a 1 g portion of catalyst was placed in the constant temperature area of the stainless-steel tubular reactor (inner diameter = 12 mm, length = 560 mm). The reactor was then heated to the target temperature (450, 500–550 °C) at a rate of 10 °C/min under a 30 mL/min  $\text{N}_2$  flow. After a constant temperature was obtained, oleic acid was injected into the reactor at a rate of 0.04 mL/min. The gaseous products were analyzed using an online gas chromatograph (GC; GC-7920, Hui Fen Co., Ltd, Shandong, China) equipped

with HP-AL/KCL (30 m × 0.530 mm × 15 μm, the type of stationary phase is Al<sub>2</sub>O<sub>3</sub>, Agilent Technologies, USA), 15–1 (3 mm × 1.5 m, the type of stationary phase is carbon molecular sieves, Hui Fen, China), and 15–5 (3 mm × 1 m, the type of stationary phase is 5 A Molecular Sieve, Hui Fen, China) columns together with a flame ionization detector (FID) and thermal conductivity detector. Using this instrumentation, the amounts of H<sub>2</sub>, CO, CO<sub>2</sub>, CH<sub>4</sub>, C<sub>2</sub>–C<sub>4</sub> olefins, and C<sub>2</sub>–C<sub>4</sub> alkanes were analyzed online. The yield of a given gaseous product,  $y(i)$ , was calculated according to the equation

$$y(i) = \frac{Q \times V(i) \times M(i) \times 273.15}{22.4 \times G \times T_e \times 1000} \times 100\%.$$

$i$ : gas product;  $Q$ : gas volume, L;  $V(i)$ : volume percentage of gas substance in gas product, %;  $G$ : feed amount, kg;  $T_e$ : room temperature, K.

The liquid phase products were collected in batches from a cold well in the lower part of the reactor. The BTX generated from each reaction were analyzed using a GC (GC-7920, Hui Fen Co., Ltd, Shandong, China) equipped with a WAX capillary column (30 m × 0.25 mm × 0.25 μm, the type of stationary phase is polyethylene glycol, Kromat Corporation, USA) and an FID. The selectivity of BTX,  $S(j)$ , was calculated according to the equation

$$S(j) = \frac{\text{Mass of BTX}}{\text{Mass of all liquid products}} \times 100\%.$$

The amount of unconverted oleic acid in each reaction mixture was determined using a GC (SCION, Tianmei Science Instrument Co., Ltd. Shanghai, China) equipped with an AB-5 capillary column (30 m × 456 C × 0.25 μm, the type of stationary phase is 5% phenyl, 95% methylpolysiloxane, bonded and crosslinked, Abel Industries, Canada) and an FID. The conversion of oleic acid was calculated as

$$C = (1 - \text{Mass of unconverted oleic acid}) \times 100\%$$

## 3 Results and Discussion

### 3.1 Characterization of the Catalysts

#### 3.1.1 Effect of Crystallization time

Figure 1 shows the XRD patterns of the NZSM-5-10/5 products prepared with different crystallization times. A crystallization time of 6 h generated an aluminosilicate. In contrast, the 9 h specimen produced clear peaks characteristic of an MFI topological structure at  $2\theta$  values of 7.8°, 8.7°, 23.1°, 23.8°, and 24.3°, corresponding to the (101), (111), (501), (303), and (313) crystal planes, respectively [29]. As the crystallization time was extended, the intensity of these peaks gradually increased, with the highest intensity obtained at 144 h. Further increases in the crystallization time to between 144 and 216 h did not lead to any further significant increases. As can be seen from Fig. S1 and Table S1, the conversion from the aluminosilicate to the zeolites has an induction period of about 9 h, followed by rapid crystallization with the full crystallization reached at about 144 h.

Figure 2 presents SEM images of the NZSM-5-10/5 samples synthesized using various crystallization times, which can be divided into five stages. In the first stage (representing an amorphous solid cogel), Al-enriched amorphous colloidal silica (ACS) aggregates were formed and the dissolution of this ACS produced an aluminosilicate gel with low content in tetrapropylammonium (TPA) (the primary amorphous phase). Further dissolution of the ACS generated worm-like and panel-like morphologies connected through undissolved ACS (the secondary amorphous phase). In the second stage, which occurred after 6 h, the ACS continued to dissolve to form individual worm-like particles. In the third stage (6–12 h), these particles gradually aggregated and formed a third amorphous phase, referred to here as condensation aggregates. After the generation of zeolite nuclei inside

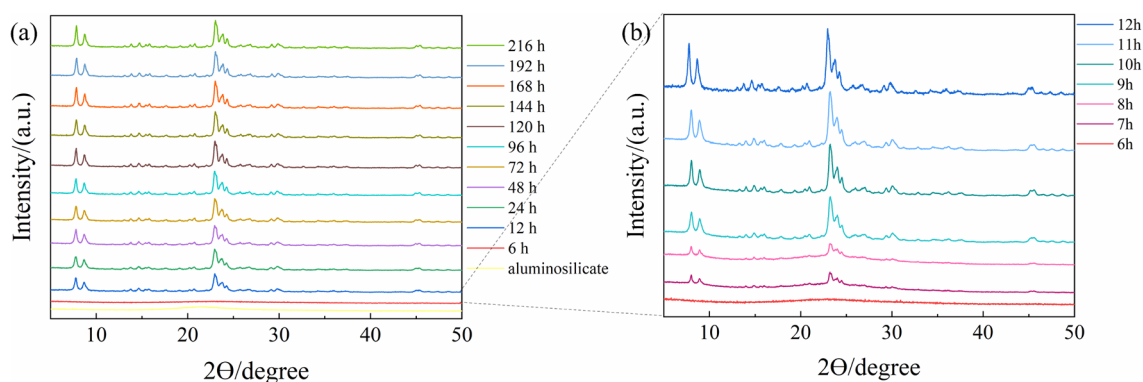
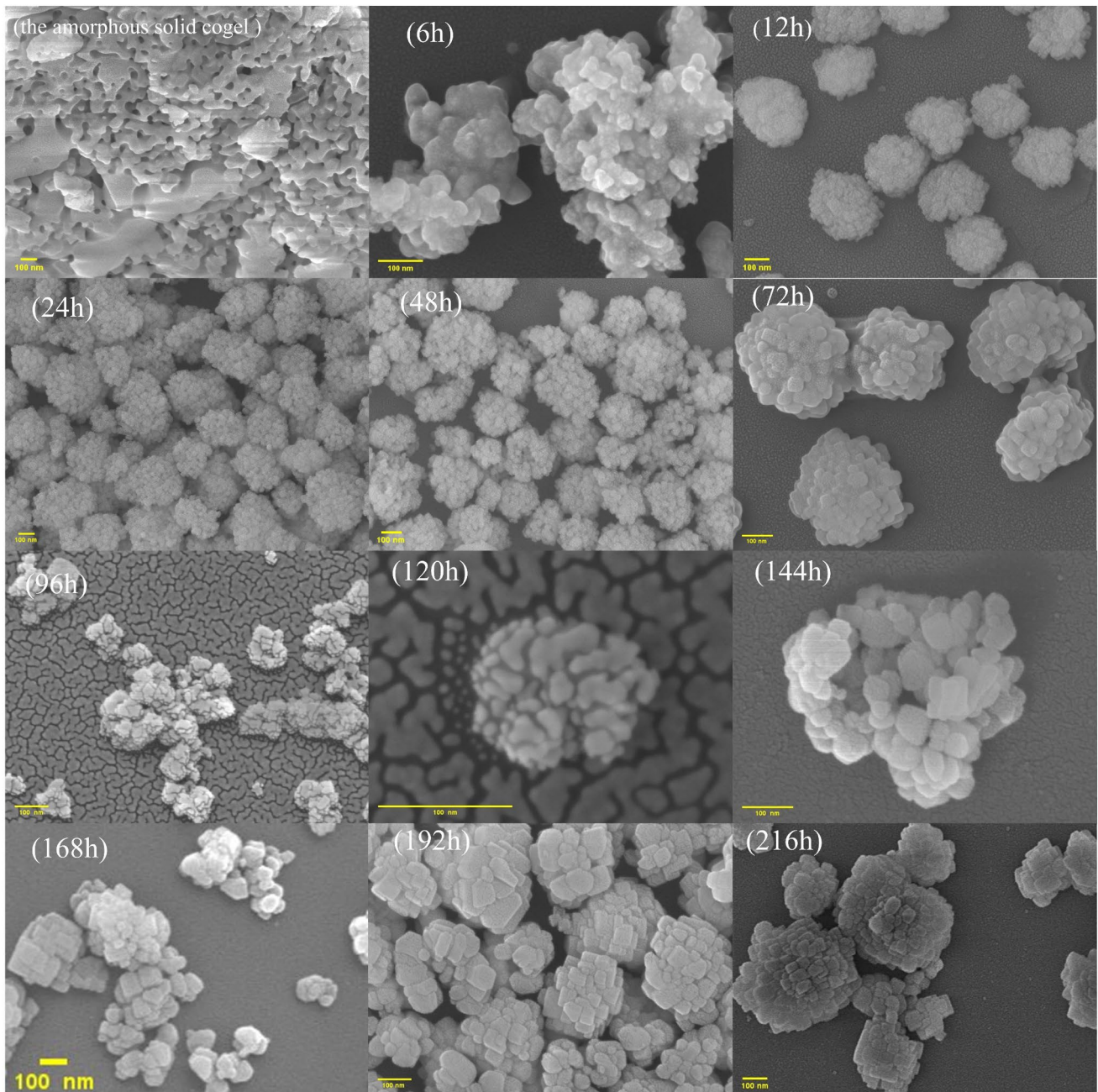


Fig. 1 XRD patterns of NZSM-5-10/5 with different crystallization times



**Fig. 2** SEM images of NZSM-5-10/5 with different crystallization times. The scale bars in the images represent 100 nm

these aggregates, the aggregates collapsed and spherical polycrystalline aggregates (PAs) were produced around the individual zeolite nuclei. These aggregates ranged in size from 150 to 400 nm, in agreement with the results reported by Ren et al. [30] The HRTEM image obtained after 12 h and the selected area electron diffraction (SAED) pattern of the corresponding region (Fig. S2) exhibited clear lattice fringes and multiple single-crystal diffraction rings. These results indicated that the ZSM-5 sample was crystalline [31]. In the fourth stage (12–144 h), the size of the PAs did not

change as the crystallization time was extended. However, the size and morphological features of the particles that made up these PAs changed significantly. Specifically, the crystals around the periphery of each PA became larger and the crystalline morphology became more pronounced. In particular, at 144 h, a single crystal with a size of approximately 50 nm appeared. Because silicon and aluminum were consumed during the first three stages, the reaction solution became less saturated and the progression of the reaction was relatively slow. In the fifth stage (144–216 h),

the individual crystals that made up the PAs continued to grow as the crystallization time was extended. The crystals became more compact and the PAs increased in size from 150–400 nm to 460–750 nm. Because the system did not contain amorphous substances that could be used to feed the reaction at this stage (meaning aluminosilicate gel), the particle growth over this time span is attributed to the dissolution and regrowth of some crystals. These results confirm that crystallization time was an important factor affecting crystal morphology.

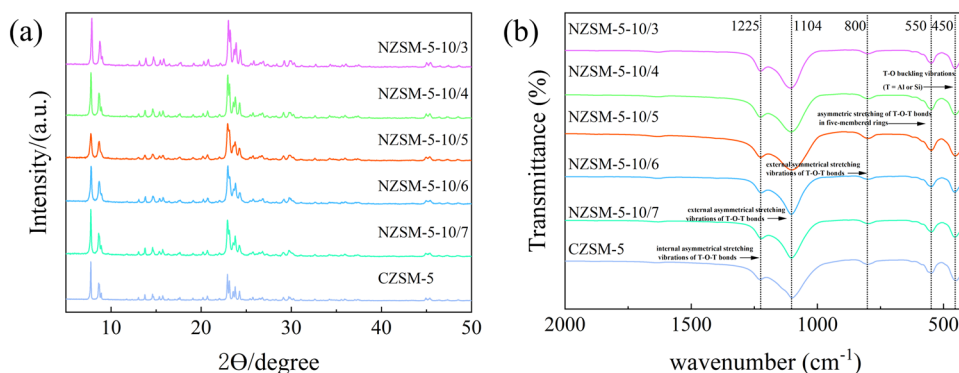
### 3.1.2 Effects of the Si/TPAOH Molar Ratio

Figure 3a presents the XRD patterns obtained from the NZSM-5 samples produced using a crystallization time of 144 h while varying the Si/TPAOH molar ratio. The crystallinity was calculated and listed in Table 1. Each of these specimens evidently had a typical MFI topology. All the NZSM-5 samples were highly crystalline, and NZSM-5-10/3 and NZSM-5-10/4 were slightly more crystalline than the other samples, probably because of their low TPAOH concentrations, producing a moderately alkaline synthetic zeolite, which was conducive to crystal formation. Karimi et al. [24] showed that low and moderate template concentrations were conducive to the synthesis of highly crystalline ZSM-5 zeolite particles. Of course, an excessively low TPAOH content was not conducive to ZSM-5 zeolite crystal formation. For example, CZSM-5's Si/TPAOH molar ratio was only 10/1.7, meaning that CZSM-5 was less crystalline than all the NZSM-5 samples. In addition, the higher aging temperature and shorter crystallization and aging times affected CZSM-5's crystallinity. According to the Scherrer equation [32], the crystal size initially decreased and then increased with changes in the Si/TPAOH ratio such that the crystal size was the smallest at a ratio of 10/5. Figure 3b provides the FTIR spectra of the NZSM-5 samples. Each of these materials produced peaks at 450, 550, 800, 1104, and 1225  $\text{cm}^{-1}$ . The peak at 450  $\text{cm}^{-1}$  was derived from T–O buckling vibrations (T = Al or Si) while that at 550  $\text{cm}^{-1}$  was attributed to the asymmetric stretching of

T–O–T bonds in five-membered rings. The peaks at 800, 1104, and 1225  $\text{cm}^{-1}$  resulted from external symmetrical, external asymmetrical and internal asymmetrical stretching vibrations of the zeolite [33, 34]. These results indicate that the amount of TPAOH in the reaction mixture had little effect on the NZSM-5 framework structure.

Figure 4 shows the TEM images acquired from the NZSM-5 samples. Figure 4a1–c1 demonstrate that, as the Si/TPAOH ratio was changed from 10/3 to 10/5, the number of large crystals decreased whereas more small crystals were produced. At a ratio of 10/5, the large crystals in the sample basically disappeared. Figure 4d1 and e1 indicate that the 10/6 and 10/7 samples comprised chip-like rectangular crystals that formed microspheres. Figure 4a2 to c2 confirm the presence of numerous intergranular mesopores in the 10/3, 10/4, and 10/5 specimens that were generated by the stacking and aggregation of nanoparticles of different sizes. In addition, Fig. 4c2 shows that the NZSM-5-10/5 tends to aggregate into nanoscale aggregates due to its high surface Gibbs energy [35]. These aggregates were loosely stacked on top of one another with obvious spaces between the individual crystals. Because the 10/5 specimen had smaller crystal sizes, it contained a greater number of intergranular mesopores compared with the 10/3 and 10/4 samples. From Fig. 4d2 and e2 it is apparent that the 10/6 and 10/7 materials were assembled from chip-like rectangular crystals that formed zeolite microspheres. This morphology was similar to that of ZSM-5-BC zeolite microspheres prepared by Ocampo et al. [36] The edges of these microspheres were loosely assembled and the NZSM-5-10/7 was denser than the other products. Interestingly, the HRTEM images in Fig. 4a3 to e3 establish that each nanoscale crystallite generated very clear lattice fringes and so was highly crystalline. Figure 4a2, b2, f1, and g1 show that the NZSM-5-10/3 and NZSM-5-10/4 samples all exhibited clear lattice fringes and that these lattice fringes had equivalent orientation. This orientation extended throughout the whole of each zeolite particle, suggesting that the nano-crystallites in these particles underwent intergrowth in an ordered manner during crystallization. Figure 4a3, b3, f3, and g3 show the micropores

**Fig. 3** XRD patterns (a) and FTIR spectra (b) of NZSM-5 and CZSM-5



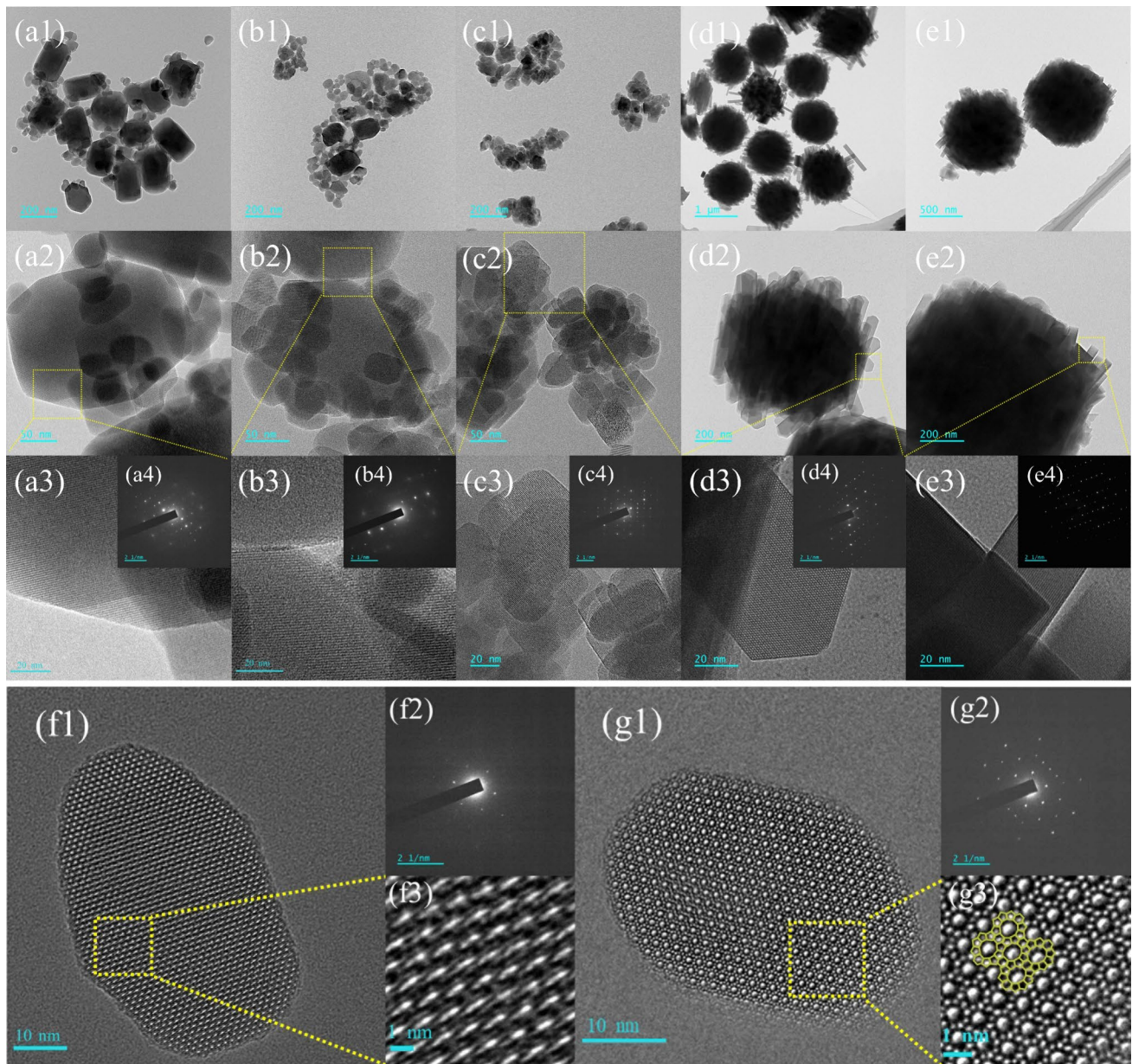


**Fig. 4** TEM, high-resolution TEM (HR-TEM) images and selected area electron diffraction (SAED) of NZSM-5: **a, f** NZSM-5-10/3, **b, g** NZSM-5-10/4, **c** NZSM-5-10/5, **d** NZSM-5-10/6, **e** NZSM-5-10/7

and intergranular mesopores in the zeolites. These pores would be expected to promote the migration of reactants, thus enhancing catalytic performance. The corresponding SAED patterns (Fig. 4a4 to e4) exhibit periodic diffraction spots throughout each particle. These results provide evidence that the MFI framework had a single crystal structure.

Figure 5 shows the SEM images and particle size distributions of the NZSM-5 products. Figure 5a–e indicate that varying the Si/TPAOH molar ratio changed the NZSM-5 from single crystals to loose polycrystalline aggregates to zeolite microspheres made of chip-like rectangular crystals.

From Fig. 5f, it is evident that the CZSM-5 particles had typical coffin-like shapes with an average particle size of approximately 1.6  $\mu\text{m}$ . At a ratio was 10/3, the NZSM-5 particle size was on the order of 200 nm with a small number of particles having sizes of less than 100 nm. Using a ratio of 10/4 generated NZSM-5 particles with sizes close to 100 nm along with some 50 nm particles attached to the surfaces of the larger particles. This outcome suggests that some of the larger particles were dissolved. A ratio of 10/5 reduced the number of large particles (approximately 100 nm in size) whereas the sizes of the smaller particles did not change



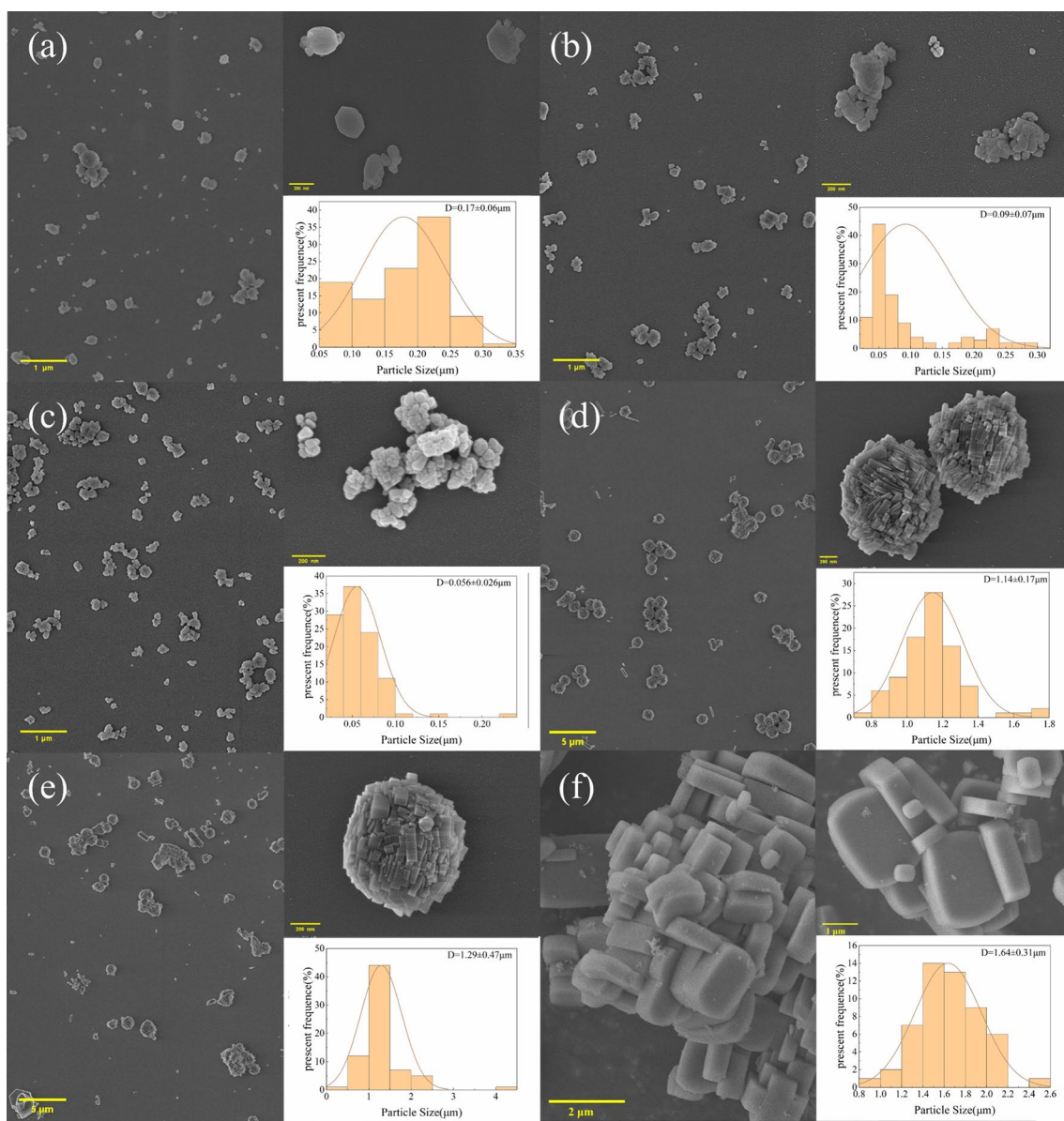


**Fig. 5** SEM images and particle size distributions of NZSM-5: **a** NZSM-5-10/3, **b** NZSM-5-10/4, **c** NZSM-5-10/5, **d** NZSM-5-10/6, **e** NZSM-5-10/7, **f** CZSM-5

significantly. However, more small particles were observed and more intergranular pores formed by the loose aggregation of nanocrystals appeared. As the amount of TPAOH in the reaction mixture was increased, the particle size of the zeolite decreased, which was consistent with the XRD results. The concentration of  $\text{TPA}^+$  had a significant effect on the formation of crystal nuclei such that a low concentration provided only a small number of such nuclei [30]. Higher  $\text{TPA}^+$  concentrations favored the formation of nuclei but did not promote growth, leading to the formation of small or ultra-small crystals [37]. Because of the instability of the monodisperse nanocrystals, these small or ultra-small nanocrystals tended to agglomerate so as to reduce surface

energy, forming polycrystalline aggregates. Consequently, increasing the TPAOH concentration in the gel precursor accelerated the nucleation rate of the crystals, resulting in the single crystal ZSM-5-10/5 aggregates described above. A ratio of 10/6 gave NZSM-5-10/6 having an average particle size of 1.1  $\mu\text{m}$ . This material assembled into zeolite microspheres having a uniform particle size distribution and based on chip-like rectangular crystals. Chu et al. [38] proposed that these rectangular crystals were produced by a special zeolite growth mechanism related to the hierarchical structure of the assembled gel spheres as well as the specific crystal growth behavior. Therefore, the appearance of this NZSM-5-10/6 morphology may have been caused by the

use of a higher TPAOH concentration that promoted unusual growth behavior. At a ratio of 10/7, the zeolite microspheres were more densely assembled at the particle edges.

Figure 6 shows the  $N_2$  adsorption/desorption isotherms and corresponding pore size distribution curves for the NZSM-5 samples. Each of these materials and the CZSM-5 generated a type IV isotherm. In addition, the extent of nitrogen adsorption increased sharply in the low-pressure region ( $p/p_0 \leq 0.1$ ), reflecting the abundance of micropores in all samples. In the high-pressure region ( $p/p_0 > 0.9$ ), the adsorption amounts increased significantly and a narrow hysteresis loop appeared, indicating that intergranular mesopores were formed by particle accumulation [39]. As can be seen from Table 1, a ratio of 10/3 gave a low external specific surface area as a consequence of the generation of large particles. At ratios of 10/4 and 10/5, both the external and total specific surface areas increased because of decreases in the particle size and increases in the number of intergranular mesopores formed by particle accumulation. At a ratio of 10/6, the total and external specific surface areas were significantly reduced

and Fig. 6a also shows the gradual disappearance of the hysteresis loop in the region of high pressure ( $p/p_0 > 0.9$ ). This outcome suggests that the intergranular mesopores formed by particle accumulation were almost gone. The SEM images also confirm the aggregation and assembly of particles. At a ratio of 10/7, the external and total specific surface areas of the sample were slightly reduced and the SEM images show that the crystal assembly was more dense. The pore size distribution (Fig. 6b) confirms that the NZSM-5 zeolites made with different Si/TPAOH molar ratios contained numerous micropores. In addition, the NZSM-5-10/3, NZSM-5-10/4, and NZSM-5-10/5 samples had pore size distributions centered at 40, 55, 70, and 93 nm, indicating that their pore systems were hierarchical. Mercury intrusion porosimetry was used to measure the distribution of pores larger than 5 nm, as shown in Figure S3. Macropores were present in all the samples, indicating that during the synthesis of hierarchical zeolite materials under certain conditions, not only mesopores but also macropores were formed [40]. In addition, small-particle samples, such as NZSM-5-10/3,

**Fig. 6**  $N_2$  adsorption/desorption isotherm (a) and corresponding pore size distribution curves (b) of NZSM-5 and CZSM-5

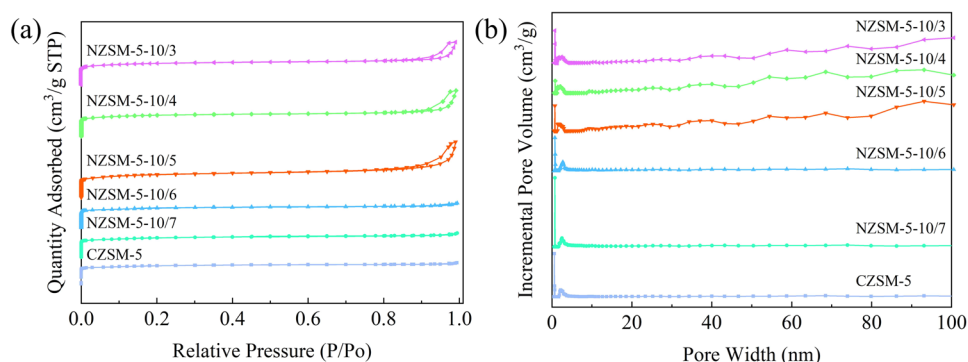


**Table 1** Textural properties of NZSM-5 and CZSM-5

Samples	Surface Area (m <sup>2</sup> /g)			Pore Volume (cm <sup>3</sup> /g)			Average Pore Size (nm)	Crystallinity <sup>h</sup> (%)
	S <sub>BET</sub> <sup>a</sup>	S <sub>micro</sub> <sup>b</sup>	S <sub>ext</sub> <sup>c</sup>	V <sub>total</sub> <sup>d</sup>	V <sub>micro</sub> <sup>e</sup>	V <sub>meso</sub> <sup>f</sup>		
NZSM-5-10/3	350	231	119	0.35	0.12	0.23	16.6	103
NZSM-5-10/4	384	241	143	0.42	0.13	0.29	18.4	103
NZSM-5-10/5	392	235	157	0.46	0.13	0.33	16.9	100
NZSM-5-10/6	332	215	117	0.21	0.12	0.09	6.6	101
NZSM-5-10/7	329	214	115	0.20	0.11	0.09	5.2	98
CZSM-5	295	202	93	0.18	0.11	0.07	4.3	81

<sup>a</sup>S<sub>BET</sub> determined by the BET method

<sup>b</sup>Calculated using t-plot method

<sup>c</sup>S<sub>ext</sub> = S<sub>BET</sub> - S<sub>micro</sub>

<sup>d</sup>Obtained from the amount adsorbed

<sup>e</sup>Calculated using t-plot method

<sup>f</sup>V<sub>meso</sub> = V<sub>total</sub> - V<sub>micro</sub>

<sup>g</sup>Calculated using the Barrett-Joyner-Halenda method

<sup>h</sup>The relative crystallinity degree was evaluated by the summation of areas of 5 the most intensive peaks

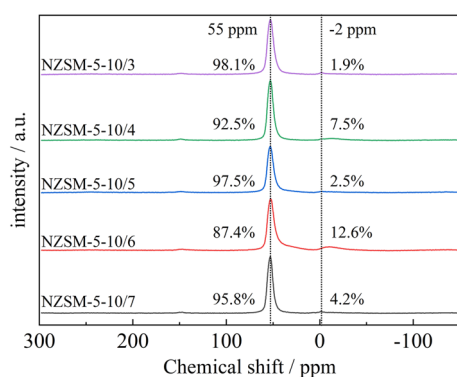


**Fig. 7**  $^{27}\text{Al}$  MAS NMR spectra of NZSM-5

NZSM-5-10/4, and NZSM-5-10/5, showed obvious pore size distributions in two regions, especially below 100 nm. Larger-particle samples, such as NZSM-5-10/6, NZSM-5-10/7, and CZSM-5, only contained pores larger than 100 nm. Table S2 lists the samples' macropore volumes. The influences of the pore size distribution and crystal size on the samples' macropore volumes were rather complex. The smallest-particle sample (NZSM-5-10/3) and macropore structures containing substantially larger pores (NZSM-5-10/6 and NZSM-5-10/7) showed higher macropore volumes.

**Fig. 8**  $\text{NH}_3$ -TPD curves (a) and Py-IR spectra (b) of NZSM-5 and CZSM-5

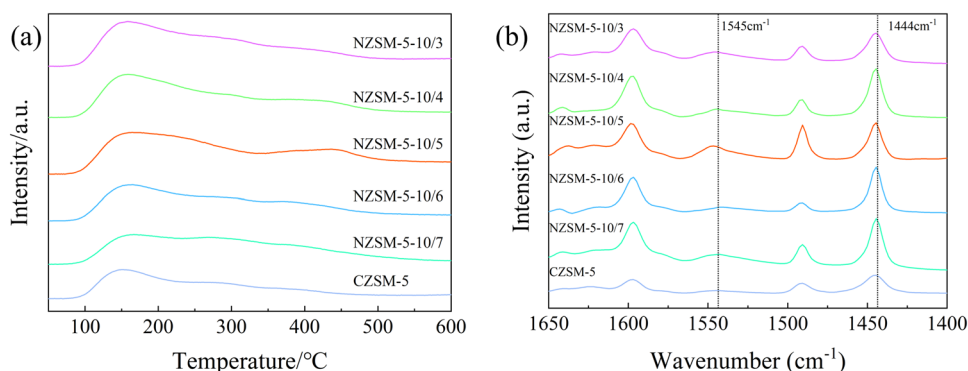


**Table 2** Acidity properties of NZSM-5 and CZSM-5 measured by  $\text{NH}_3$ -TPD and Py-IR

Samples	Acid amount (mmol/g)			Acidity by type (mmol/g)			L/(B+L)
	Weak	Strong	Total	B <sup>a</sup>	L <sup>b</sup>	B+L	
NZSM-5-10/3	0.71	0.03	0.74	0.23	0.18	0.41	0.44
NZSM-5-10/4	0.78	0.07	0.85	0.14	0.27	0.41	0.65
NZSM-5-10/5	0.83	0.11	0.94	0.23	0.21	0.44	0.47
NZSM-5-10/6	0.64	0.02	0.66	0.07	0.22	0.29	0.77
NZSM-5-10/7	0.55	0.02	0.57	0.21	0.26	0.47	0.56
CZSM-5	0.50	0.02	0.52	0.04	0.15	0.19	0.78

<sup>a</sup>Amounts of Brønsted acid sites

The absorption coefficient of Brønsted acid sites = 1.88

<sup>b</sup>Amounts of Lewis acid sites

The absorption coefficient of Lewis acid sites = 1.42

Figure 7 provides the  $^{27}\text{Al}$  MAS NMR spectra of the NZSM-5 materials. Each of the samples produce a main peak at approximately 55 ppm and a minor peak at approximately  $-2$  ppm. The former was attributed to tetrahedrally coordinated Al atoms within the framework structure whereas the latter was related to octahedrally coordinated Al situated in the extra framework [35]. In each case, no significant extra-framework Al signal was observed, indicating that the majority of the Al atoms were located within the framework. The peak areas of the NZSM-5-10/3, NZSM-5-10/4, NZSM-5-10/5, NZSM-5-10/6, and NZSM-5-10/7 samples at  $-2$  ppm were 1.9%, 7.5%, 2.5%, 12.6%, and 4.2%, respectively.

Figure 8a shows the  $\text{NH}_3$ -TPD curves acquired from the NZSM-5 samples. The peaks in the ranges of  $50$ – $350$  °C and  $350$ – $600$  °C correspond to weak and strong acid sites, respectively. With decreasing crystal size (CZSM-5 > NZSM-5-10/7 > NZSM-5-10/6 > NZSM-5-10/3 > NZSM-5-10/4 > NZSM-5-10/5), the acidic sites' concentration gradually increased (Table 2). Although the concentration of the weakly acidic sites negligibly increased, that of the strongly acidic sites substantially increased. For example, the concentration of the strongly acidic sites in NZSM-5-10/5 was about 2–6 times higher than those of the strongly acidic sites in the other samples. On the one hand,

the crystal size reduction increased the zeolite's specific surface area (which provided more adsorption sites for probe molecules ( $\text{NH}_3$ )). On the other hand, the reduced zeolite size shortened both the straight and sinusoidal channels in ZSM-5, which was conducive to  $\text{NH}_3$  molecular diffusion into the pores, adsorption, desorption, and diffusion out of the pores. Because of the high diffusion resistance of sinusoidal channel, the shortened sinusoidal channel substantially affected the number of adsorbed/desorbed  $\text{NH}_3$  molecules. Shiralkar et al. [41] also observed that for ZSM-5 zeolites possessing the same Si/Al ratio and different crystal sizes, the acidic site density gradually increased with decreasing crystal size, and the density of the strongly acidic sites substantially increased. For example, the crystallite size of sample 1 was only 1/5–1/9 of those of samples 3 and 4, and the area of sample 1's strongly acidic sites was more than 10 times larger than those of sample 3 and 4's strongly acidic sites. Figure 8b provides the Py-IR spectra of the same materials. The peak at  $1545\text{ cm}^{-1}$  is related to the formation of  $\text{PyH}^+$  via protonation at B acid sites whereas that at  $1444\text{ cm}^{-1}$  is assigned to pyridine coordinated with L acid sites in the zeolite [34]. It can be seen that all samples contained B and L acid sites. The amounts of the individual B and L acid sites were calculated from the integrated intensities of the  $1545$  and  $1444\text{ cm}^{-1}$  bands, respectively, and the results are provided in Table 2. The  $L/(B+L)$  ratio of these products increased in the order of  $\text{NZSM-5-10/3} < \text{NZSM-5-10/5} < \text{NZSM-5-10/7} < \text{NZSM-5-10/4} < \text{NZSM-5-10/6}$ . This result was consistent with the amounts of extra-skeletal Al species in the samples as determined using  $^{27}\text{Al}$  MAS NMR (Fig. 7). This finding suggests that the L acid sites were primarily associated with extra-framework Al, in agreement with results reported by Zhang et al. [42] Among the NZSM-5 samples, NZSM-5-10/6 was the least acidic because its B acidic site concentration was much lower than those of the other NZSM-5 samples. For synthesizing the NZSM-5 zeolite, although aluminum nitrate (the aluminum species) existed as  $\text{Al}[(\text{OH}_2)_6]^{3+}$ , TPAOH first converted  $\text{Al}[(\text{OH}_2)_6]^{3+}$  to tetraordinated  $\text{Al}(\text{OH})_4^-$  before it could

interact with the silicon species. In NZSM-5, the transformation from  $[\text{Al}(\text{OH}_2)_6]^{3+}$  to  $\text{Al}(\text{OH})_4^-$  formed more Al pairs, and the more Al pairs formed, the higher and lower the extra-framework's and framework's Al contents are, respectively. The literature shows that with increasing alkalinity, the Al pairs' content follows a volcanic distribution [43]. In this work, with increasing Si/TPAOH molar ratios (alkalinity), the extra-framework's Al content basically followed a volcanic distribution. At a Si/TPAOH molar ratio of 10/6, because the extra-framework's Al content was maximized (Fig. 7), the framework's Al content was minimized; that is, because the B acidic sites' concentration was minimized, the acidity was minimized, as measured using pyridine adsorption infrared (Py-IR) spectroscopy. In CZSM-5, the B acidic sites' concentration was very low, probably because the crystallization time of CZSM-5 was shorter than that of NZSM-5 zeolite. Short crystallization time would lead to its slow of bridged  $-\text{Al}(\text{OH})\text{Si}-$  in the framework, resulting in octahedral non-framework Al did not fully transform to tetraordinated Al of CZSM-5, eventually reducing both the framework's Al content and B acidic sites' concentration [44].

## 3.2 Catalyst Performance

### 3.2.1 Cracking of Oleic Acid with Different Catalysts

Figure 9a shows that the yields of gaseous products obtained using the NZSM-5 specimens as catalysts were basically higher than that generated by the CZSM-5. In the NZSM-5 samples, the B acidic sites' concentrations were substantially higher than those in CZSM-5, which was favorable for cracking oleic acid. In addition, the NZSM-5 specimens possessed abundant intergranular mesopores and external specific surface areas, which were conducive to oleic acid's molecular diffusion and contact with the acidic sites, thus promoting oleic acid cracking. CZSM-5 mainly possesses a microporous structure, and although oleic acid can diffuse in micropores, the diffusion resistance is high. In addition,

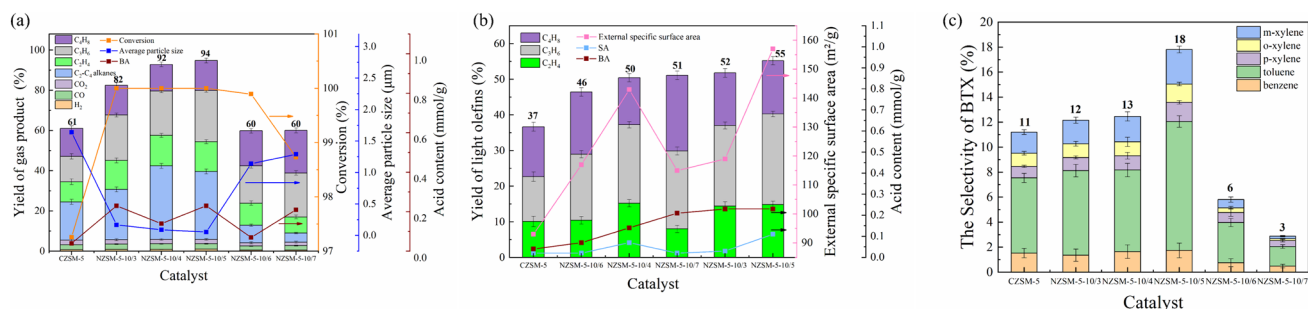


**Fig. 9** Catalytic cracking of oleic acid with different catalysts: **a** yield of gas product and oleic acid conversion, **b** yield of LOs, **c** selectivity of BTX. Reaction conditions: reaction temperature, 500 °C; oleic acid flow rate, 0.04 mL/min;  $\text{N}_2$  flow rate, 30 mL/min

large CZSM-5 particles prolong oleic acid's residence in pores, which easily leads to overreaction and the production heavy hydrocarbons and coke. As the particle sizes of the NZSM-5 specimens decreased, the yields increased from 60 to 94% with the NZSM-5 having a Si/TPAOH molar ratio of 10/5 giving the highest yield of 94%. The NZSM-5-10/5 had the smallest average particle size (0.056  $\mu\text{m}$ ) and this reduced steric hindrance while shortening the residence time of molecules in the pores. This characteristic limited secondary reactions of the primary products. This material also had abundant intergranular mesopores and so had the largest external specific surface area (157  $\text{m}^2/\text{g}$ ). The abundant externally accessible active sites on this product were conducive to the transfer and cracking of macromolecules. The oleic acid conversion obtained using the CZSM-5 catalyst was approximately 97% whereas the conversion percentages provided by all the NZSM-5 catalysts were close to 100%. The external specific surface areas of the NZSM-5 samples were much larger than that of the CZSM-5, and this factor increased the degree of contact between oleic acid and active sites. Reddy et al. [45] investigated the influence of the ZSM-5 particle size on the catalytic cracking of n-heptane and found that small ZSM-5 particles exhibited good catalytic activity because the short pore structure of the small ZSM-5 particles was conducive to the diffusion of reactants and products.

As shown in Fig. 9b, the concentration of B acid sites increased from 0.04 mmol/g in the case of the CZSM-5 to 0.23 mmol/g in the case of the NZSM-5-10/5. The corresponding yield of LOs increased from 37 to 55%. The protons provided by B acid sites were capable of forming an alkanium ion supposed transition, which in turn collapsed to form small molecules such as methane and ethane as well as carbenium ions [46, 47]. These carbenium ions returned protons to the catalyst via dehydrogenation to form alkenes [48]. However, an overly high B acid site concentration promoted secondary reactions such as hydrogen transfer and the aromatization of olefins [49]. In addition, as the concentration of strong acid sites of the catalyst increased from 0.02 mmol/g (CZSM-5) to 0.11 mmol/g (NZSM-5-10/5), the yield of LOs changed from 37 to 55%, indicating that strong active sites contributed to the production of LOs. Shao et al. [50] reported the preparation of LOs from cellulose catalyzed by a ZSM-5 zeolite and showed that strong acid sites promoted this reaction. The external specific surface area of the catalyst increased from 93  $\text{m}^2/\text{g}$  (for the CZSM-5) to 157  $\text{m}^2/\text{g}$  (for the NZSM-5-10/5) while the yield of LOs increased from 37 to 55%. The large external specific surface area of the latter promoted interactions between intermediate products and acidic sites, accelerating the deoxidation process for the production of olefins. More importantly, the small particle size of the NZSM-5-10/5 resulted in shorter diffusion paths such that the LOs more readily diffused out

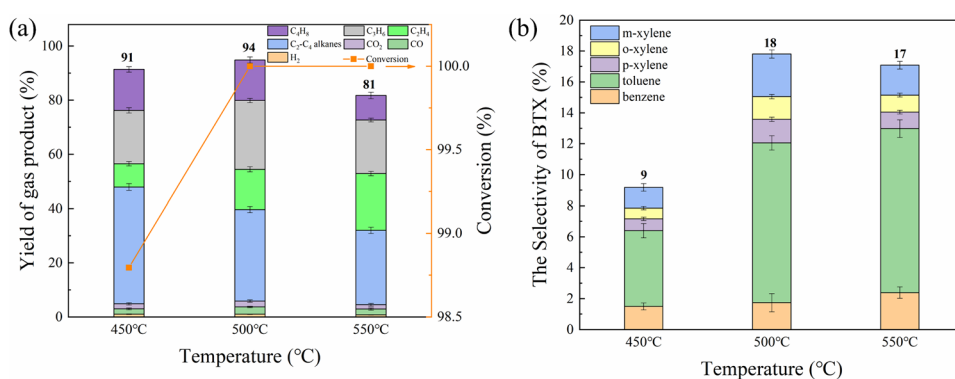
of the material and avoided deep reactions. The NZSM-5-10/5 had the smallest average particle size (56 nm) and a large average pore size (16.9 nm). These factors reduced the degree of steric hindrance and internal diffusion resistance impacting the oleic acid cracking reaction. This material also contained many B acid sites and strong acid sites and so gave a high yield of LOs.

As shown in Fig. 9c, in CZSM-5, the strongly acidic sites' concentration increased from 0.02 to 0.11 mmol/g in NZSM-5-10/5, and the selectivity of BTX increased from 11 to 18% for the liquid product because numerous strongly acidic sites promote the cracking, hydrogen transfer, and aromatization of the oleic acid, resulting in the increase of BTX selectivity in liquid phase products. Che et al. [51] analyzed the effects of Zn-, Fe-, Ca-, Ce-, and La-modified ZSM-5 on biomass's catalytic pyrolysis, and the results showed that the BTX yield was positively correlated with the catalysts' strongly acidic site contents. In addition, a higher pore volume was an important factor to improve the BTX yield. The NZSM-5-10/5 pore volume (0.46  $\text{cm}^3/\text{g}$ ) was much higher than that of CZSM-5 (0.18  $\text{cm}^3/\text{g}$ ), which was conducive to oleic acid diffusion and cracking. Che et al. [52] introduced additional mesopores to ZSM-5 zeolite and found that they promoted the cracking of bulky oxygenates and suppressed polymerization on the ZSM-5 surface, generating more aromatic products. Although the pore structure and volume of NZSM-5-10/6 and NZSM-5-10/7 were similar to those of CZSM-5, their BTX selectivities were much lower than that of CZSM-5 because NZSM-5-10/6 and NZSM-5-10/7 possessed more compact structures, which inherently hindered the entry of the reactants to the zeolite, thus affecting BTX formation.

### 3.2.2 Effect of Reaction Temperature on Catalyst Performance

Figure 10a shows that the highest gaseous product yield of 94% was obtained at a reaction temperature of 500  $^{\circ}\text{C}$ . In contrast, at 550 and 450  $^{\circ}\text{C}$ , the yields were 81% and 91%, respectively. High temperatures could cause the oleic acid to be partially converted into coke and deposited on the surface of the catalyst, resulting in a decrease in catalyst activity [15]. In addition, the conversion of oleic acid was 100% at reaction temperatures above 500  $^{\circ}\text{C}$  but slightly lower (98.8%) at 450  $^{\circ}\text{C}$ . At 500  $^{\circ}\text{C}$ , the highest yield of LOs of 55% was observed while the trial at 550  $^{\circ}\text{C}$  gave a value of 50%. This decrease in the yield of LOs occurred because the higher temperature promoted the secondary cracking of LOs and accelerated the coking reactions, thereby inhibiting the formation of LOs [53]. The data also show that increasing the reaction temperature elevated the ethylene yield while the yields of propylene and butylene first increased and then decreased. The monomolecular cracking mechanism

**Fig. 10** Catalytic cracking of oleic acid with NZSM-5-10/5 at different temperatures: **a** yield of gas product and oleic acid conversion, **b** selectivity of BTX. Reaction conditions: oleic acid flow rate, 0.04 mL/min; N<sub>2</sub> flow rate, 30 mL/min



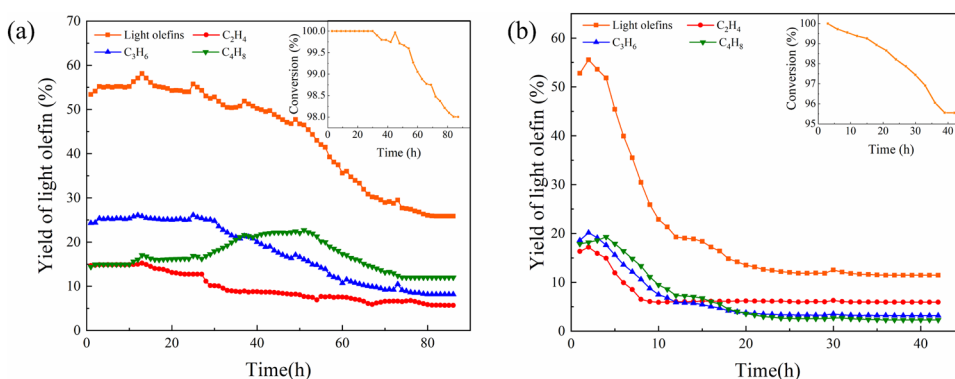
was dominant at higher temperatures, and the occurrence of secondary reactions that consumed almost no ethylene [54]. Liu et al. [55] catalyzed the pyrolysis of 1-pentene to prepare LOs using HZSM-5 zeolites treated with sodium hydroxide solutions having varying concentrations. The maximum butene yield was obtained at 500 °C and the secondary reactions of this intermediate product decreased the yield above this temperature. As shown in Fig. 10b, the highest selectivity of BTX in the liquid phase product was obtained at 500 °C and this value of 18% was much higher than that at 450 °C and 550 °C. Even so, an overly low temperature was not conducive to cracking of the oleic acid and did not promote the transformation of alkylbenzene to benzene and olefins [56]. However, an excessively high temperature accelerated the reactant coking, thereby reducing the selectivity of BTX.

### 3.3 Stability of the Catalysts

Figure 11a shows that the yield of LOs generated using the NZSM-5-10/5 remained stable for the first 10 h and then decreased. After 80 h, the yield had decreased to 26% and then remained unchanged, indicating that the catalyst was inactivated. Over the range 30–50 h, the butene yield increased to the maximum at approximately 50 h. In the initial stage, the butene produced by cracking the raw material underwent the following reactions: The butene

molecules adsorbed at B acidic sites to form C<sub>4</sub><sup>+</sup> carbenium ions, which oligomerized with other butene molecules to form C<sub>8</sub><sup>+</sup> carbenium ions (some oligomerized to form C<sub>12</sub><sup>+</sup> carbenium ions). Then, C<sub>8</sub><sup>+</sup> carbenium ions underwent beta-cleavage ( $\beta$ -scission) at weakly acidic sites (WA sites) to form C<sub>3</sub><sup>+</sup> and C<sub>5</sub><sup>+</sup> carbenium ions. Finally, C<sub>5</sub><sup>+</sup> carbenium ions further decomposed to propylene and ethene [57, 58]. These reactions mostly occurred in micropores. With prolonged reaction times, carbon deposition blocked the micropores' acidic sites, which was not conducive to the oligomerization of the butene molecules and, therefore, reduced the further conversion from butene to ethylene and propylene [59]. The gradual clogging of the micropores by coke as the reaction progressed reduced the cracking of propylene. Throughout the first 30 h, the conversion of oleic acid remained at 100% but then began to decline, reaching a minimum of 98%. Figure 11b shows that the yield of LOs generated by the CZSM-5 decreased between 2 and 25 h to a minimum of 12%, suggesting that the material had become inactivated. Primarily, the CZSM-5 zeolite is a microporous material, and micropores are blocked by condensation products much more quickly than mesopores. Additionally, coke deposition easily blocked the micropore openings and external surface region, covering the active sites [60]. Under the same conditions, the catalytic lifetime of NZSM-5-10/5 was approximately 3.2 times that of CZSM-5, indicating

**Fig. 11** Effect of reaction time on yield of LOs and oleic acid conversion: **a** NZSM-5-10/5, reaction time, 90 h; **b** CZSM-5, reaction time, 42 h. Reaction conditions: reaction temperature, 500 °C; oleic acid flow rate, 0.04 mL/min; N<sub>2</sub> flow rate, 30 mL/min



that the larger external surface area resists deactivation by considerable coke deposition.

### 3.4 Coke Analysis

Figure 12 shows the TG results obtained from the spent catalysts. The mass loss of the samples below 200 °C was attributed to the evaporation of water from the zeolite. Mass loss in the range of 200–400 °C was attributed to the oxidation of so-called soft coke while that in the range of 400–800 °C was ascribed to the oxidation of hard coke [61]. The coke content of the NZSM-5-10/5-80 (27.3%) was also significantly higher than that of the CZSM-5-25 (15.9%). The intergranular accumulation of the NZSM-5-10/5 produced a rich mesoporous structure that provided storage sites for coke and so improved the anti-coking ability of the catalyst. In addition, the numerous mesopores were also conducive to the diffusion of macromolecules in the pores and so inhibited clogging of the micropores. These effects increased the yield of gaseous products and ensured good catalytic activity. In the case of the CZSM-5, the diffusion of intermediates and products in the zeolite channels was limited because of the large particle sizes and abundant micropores that were easily clogged.

## 4 Conclusion

NZSM-5 zeolite specimens having different crystal sizes were synthesized by hydrothermal synthesis by changing the amount of TPAOH and applied to the production of LOs and BTX via the catalytic cracking of oleic acid. The effects of crystallization time on the zeolite growth process were also explored. The results showed that, with increases in the crystallization time, the zeolites gradually transitioned from amorphous to loose aggregates of crystalline particles

and then formed dense, compacted crystalline aggregates. The effects of the crystal size and acidity of the NZSM-5 on the yields of gas phase products and BTX and on the oleic acid conversion were also examined. The NZSM-5-10/5 showed the best catalytic activity based on the high B acid site concentration (0.23 mmol/g), strong acid concentration (0.11 mmol/g), large external specific surface area (157 m<sup>2</sup>/g), small particle size (an average particle size of 56 nm) and abundant intergranular mesopores of this material. At 500 °C, yield of LOs and the selectivity of BTX in liquid phase products as high as 55% and 18%, respectively, were obtained. Under the same conditions, the catalytic lifespan of NZSM-5-10/5 was approximately 3.2 times that of CZSM-5, indicating that the larger external surface area resists deactivation by considerable coke deposition. In addition, the results show that an overly high temperature (550 °C) accelerated secondary reactions, resulting in more coke deposition and thus reduced catalytic activity.

**Supplementary Information** The online version contains supplementary material available at <https://doi.org/10.1007/s10904-024-03404-w>.

**Author Contributions** All authors contributed to the study conception and design. Material preparation, data collection was performed by Hao Liu, Yanlin Wang and Wenbo Luo. The first draft of the manuscript was written by Hao Liu and Hong Yuan commented on previous versions of the manuscript and supervised the entire work. All authors read and approved the final manuscript.

**Funding** This study was supported by the National Natural Science Foundation of China (21962001), the Ningxia Key Research and Development Project of China (2023BDE03009), the Innovative Team for Transforming Waste Cooking Oil into Clean Energy and High Value-Added Chemicals of China, and the Ningxia Low-Grade Resource High Value Utilization and Environmental Chemical Integration Technology Innovation Team Project of China.

**Data Availability** The data supporting this article have been included as part of the Supplementary Information. No datasets were generated or analysed during the current study.

## Declarations

**Conflict of interest** The authors have no relevant financial or non-financial interests to disclose.

## References

1. L.Y. Du, Y.Y. Han, Y.H. Xu, *Catalysts*. **13**, 1013 (2023)
2. Q. Gong, T. Fang, Y.L. Xie, R. Zhang, M. Liu, F. Barzagli, J.H. Li, Z.H. Hu, Z.R. Zhu, *Ind. Eng. Chem. Res.* **60**, 1633–1641 (2021)
3. J. Oh, Y. Choi, J. Shin, K. Kim, J.K. Lee, *Fuel Process. Technol.* **249**, 107856 (2023)
4. H.C. Genuino, I. Muizebelt, A. Heeres, N.J. Schenk, J.G.M. Winkelman, H.J. Heeres, *Green. Chem.* **21**, 3802–3806 (2019)
5. Y.P. Li, Y. Li, X.H. Zhang, C.G. Wang, X. Li, L.L. Ma, *Int. J. Hydrogen Energ.* **46**, 3669–3683 (2021)
6. M. Fakhroleslam, S.M. Sadrameli, *Fuel*. **252**, 553–566 (2019)

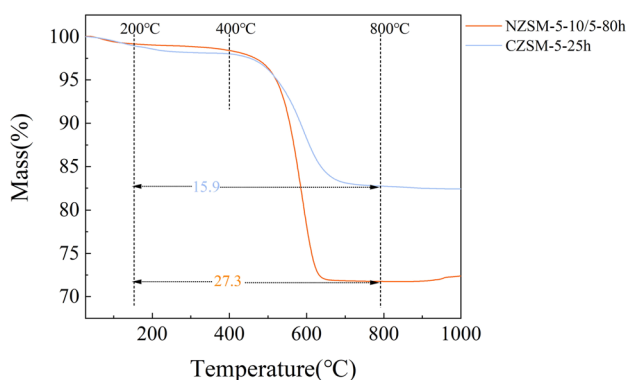


**Fig. 12** TG curves of spent catalysts for NZSM-5-10/5-80 h and CZSM-5-25 h. Reaction conditions: reaction temperature, 500 °C; oleic acid flow rate, 0.04 mL/min; N<sub>2</sub> flow rate, 30 mL/min

7. F. Wang, M.X. Zhou, X.H. Yang, L.J. Gao, G.M. Xiao, *Mol. Catal.* **432**, 144–154 (2017)
8. J.A. Botas, D.P. Serrano, A. García, R. Ramos, *Appl. Catal. B-Environ Energy.* **145**, 205–215 (2014)
9. A. Corma, G.W. Huber, L. Sauvanaud, P. O'connor, *J. Catal.* **247**, 307–327 (2007)
10. H. Chen, Q.F. Wang, X.W. Zhang, L. Wang, *Appl. Catal. B-Environ Energy.* **166**, 327–334 (2015)
11. L.J. Guan, M.Y. Liu, H.H. Liu, L. Zhang, Y.M. Zhang, Y.C. Qin, B.B. He, Y. Mei, Y. Zu, *Fuel.* **353**, 129230 (2023)
12. X. Huang, R.Z. Wang, X. Pan, C.F. Wang, M.H. Fan, Y.F. Zhu, Y.G. Wang, J. Peng, *Green. Energy Environ.* **5**, 385–393 (2020)
13. W. He, F.W. Li, Y.F. Gu, X.F. Wang, H.S. Gu, H.B. Fu, X.M. Liang, Z.X. Li, *Acs Omega.* **7**, 40520–40531 (2022)
14. X.G. Yang, F. Wang, R.P. Wei, S. Li, Y.F. Wu, P.X. Shen, H.Z. Wang, L.J. Gao, G.M. Xiao, *Micropor Mesopor Mat.* **257**, 154–161 (2018)
15. T.T. Zhao, F.W. Li, H.C. Yu, S.L. Ding, Z.X. Li, X.Y. Huang, X. Li, X.H. Wei, Z.L. Wang, H.F. Lin, *Appl. Catal. A-Gen.* **575**, 101–110 (2019)
16. N.N. Xu, D.H. Pan, Y.F. Wu, S.Q. Xu, L.J. Gao, J. Zhang, G.M. Xiao, *React. Kinet Mech. Cat.* **127**, 449–467 (2019)
17. H. Konno, T. Tago, Y. Nakasaka, R. Ohnaka, J.I. Nishimura, T. Masuda, *Micropor Mesopor Mat.* **175**, 25–33 (2013)
18. L.L. Yi, H. Liu, S.H. Li, M.Y. Li, G.Y. Wang, G.Z. Man, H. Yao, *Bioresour Technol.* **294**, 122186 (2019)
19. J.L. Xu, Z.H. Zhang, G. Wang, X.Z. Duan, G. Qian, X.G. Zhou, *Chem. Eng. Sci.* **227**, 115907 (2020)
20. A. Agarwal, S.J. Park, J.H. Park, *Fuel.* **271**, 117630 (2020)
21. J. Aguado, D.P. Serrano, J.M. Escola, J.M. Rodríguez, *Micropor Mesopor Mat.* **75**, 41–49 (2004)
22. X.F. Su, Y.L. Zhang, A.L. Maximov, K. Zhang, Q. Xin, C.Q. Feng, X.F. Bai, W. Wu, *Russ J. Appl. Chem.* **93**, 127–136 (2020)
23. Z.D. Wang, Y. Luo, X.C. Li, W.M. Yang, *J. Porous Mat.* **27**, 1329–1337 (2020)
24. R. Karimi, B. Bayati, N.C. Aghdam, M. Ejtemaee, A.A. Babaluo, *Powder Technol.* **229**, 229–236 (2012)
25. G.Q. Song, D. Xue, J.W. Xue, F.X. Li, *Micropor Mesopor Mat.* **248**, 192–203 (2017)
26. S.M. Alipour, *Chinese, J. Catal.* **37**, 671–680 (2016)
27. H. Mochizuki, T. Yokoi, H. Imai, R. Watanabe, S. Namba, J.N. Kondo, T. Tatsumi, *Micropor Mesopor Mat.* **145**, 165–171 (2011)
28. H.D. Wu, A.J. Duan, Z. Zhao, T.S. Li, R. Prins, X.F. Zhou, *J. Catal.* **317**, 303–317 (2014)
29. J. Zhou, Z.L. Hua, Z.C. Liu, W. Wu, Y. Zhu, J.L. Shi, *Acs Catal.* **1**, 287–291 (2011)
30. N. Ren, B. Subotić, J. Bronić, Y. Tang, M.D. Sikirić, T. Mišić, V. Svetličić, S. Bosnar, T.A. Jelić, *Chem. Mater.* **24**, 1726–1737 (2012)
31. F.J. Liu, T. Willhammar, L. Wang, L.F. Zhu, Q. Sun, X.J. Meng, W. Carrillo-Cabrera, X.D. Zou, F.S. Xiao, *J. Am. Chem. Soc.* **134**, 4557–4560 (2012)
32. S. Lee, M. Choi, *J. Catal.* **375**, 183–192 (2019)
33. Z.H. Zhou, X.W. Wang, J.J. Li, Y. Gao, R. Yu, R.L. Jiang, *Chem-Eur J.* **29**, e202203095 (2023)
34. C.A. Emeis, *J. Catal.* **141**, 347–354 (1993)
35. Y. Gao, G. Wu, F.W. Ma, C.T. Liu, F. Jiang, Y. Wang, A.J. Wang, *Micropor Mesopor Mat.* **226**, 251–259 (2016)
36. F. Ocampo, J.A. Cunha, M.R.D. Santos, J.P. Tessonnier, M.M. Pereira, B. Louis, *Appl Catal. A-Gen.* **390**, 102–109 (2010)
37. Y. Zhao, H.B. Zhang, P.C. Wang, F.Q. Xue, Z.Q. Ye, Y.H. Zhang, Y. Tang, *Chem. Mater.* **29**, 3387–3396 (2017)
38. N.B. Chu, J.H. Yang, C.Y. Li, J.Y. Cui, Q.Y. Zhao, X.Y. Yin, J.M. Lu, J.Q. Wang, *Micropor Mesopor Mat.* **118**, 169–175 (2009)
39. T.J. Fu, J.W. Chang, J. Shao, Z. Li, *J. Energy Chem.* **26**, 139–146 (2017)
40. O.S. Travkina, M.R. Agliullin, N.A. Filippova, A.N. Khazipova, I.G. Danilova, N.G. Grigor'Eva, N. Narender, M.L. Pavlov, B.I. Kutepov, *RSC Adv.* **7**, 32581–32590 (2017)
41. V.P. Shiralkar, P.N. Joshi, M.J. Eapen, B.S. Rao, *Zeolites.* **11**, 511–516 (1991)
42. L.W. Zhang, H.K. Zhang, Z.Q. Chen, Q. Ning, S.Y. Liu, J. Ren, X.D. Wen, Y.W. Li, *Catal. Sci. Technol.* **9**, 7034–7044 (2019)
43. M.J. Xing, L. Zhang, J. Cao, Y.L. Han, F. Wang, K. Hao, L.H. Huang, Z.C. Tao, X.D. Wen, Y. Yang, Y.W. Li, *Micropor Mesopor Mat.* **334**, 111769 (2022)
44. F. Pan, X.C. Lu, T.Z. Wang, Y. Yan, *Mater. Lett.* **196**, 245–247 (2017)
45. J.K. Reddy, K. Motokura, T.-. Koyama, A. Miyaji, T. Baba, *J. Catal.* **289**, 53–61 (2012)
46. G. Caeiro, R.H. Carvalho, X. Wang, F. M.A.N.D.A. Lemos, M. Lemos, F. Guisnet, Ramôa, Ribeiro, *J. Mol. Catal. A-Chem.* **255**, 131–158 (2006)
47. F.C. Jentoft, B.C. Gates, *Top. Catal.* **4**, 1–13 (1997)
48. C. Chizallet, C. Bouchy, K. Larmier, G. Pirngruber, *Chem. Rev.* **123**, 6107–6196 (2023)
49. Y.J. Tian, X.Y. He, X.Z. Chen, C.Z. Qiao, H.Y. Wang, Z.H. Diao, G.Z. Liu, *Fuel.* **363**, 130902 (2024)
50. J. Shao, H. Jiang, M.F. Yang, J.J. Xiao, H.P. Yang, Y.Q. Chen, S.H. Zhang, H.P. Chen, *J. Anal. Appl. Pyrol.* **166**, 105628 (2022)
51. Q.F. Che, M.J. Yang, X.H. Wang, Q. Yang, L.R. Williams, H.P. Yang, J. Zou, K. Zeng, Y.J. Zhu, Y.Q. Chen, H.P. Chen, *Bioresour Technol.* **278**, 248–254 (2019)
52. Q.F. Che, M.J. Yang, X.H. Wang, Q. Yang, Y.Q. Chen, X. Chen, W. Chen, J.H. Hu, K. Zeng, H.P. Yang, H.P. Chen, *Bioresour Technol.* **289**, 121729 (2019)
53. S.Y. Liu, Y.N. Zhang, L.L. Fan, N. Zhou, G.Y. Tian, X.D. Zhu, Y.L. Cheng, Y.P. Wang, Y.H. Liu, P. Chen, R. Ruan, *Fuel.* **196**, 261–268 (2017)
54. K. Kubo, H. Iida, S. Namba, A. Igarashi, *J. Jpn Petrol. Inst.* **61**, 10–19 (2018)
55. D.Y. Liu, L.Z. Zhang, Z.Q. Qiao, Y.E. Bai, L. Zhao, J.S. Gao, C.M. Xu, *Aiche J.* **69**, e17918 (2023)
56. P. Ghorbannezhad, M.D. Firouzabadi, A. Ghasemian, P.J. de Wild, H.J. Heeres, *J. Anal. Appl. Pyrol.* **131**, 1–8 (2018)
57. X.X. Zhu, S.L. Liu, Y.Q. Song, S.J. Xie, L.Y. Xu, *Appl. Catal. A-Gen.* **290**, 191–199 (2005)
58. K.Z. Wang, J.L. Zhang, S.B. Fan, X.B. Peng, N. Tsubaki, T.S. Zhao, *New J. Chem.* **45**, 4860–4866 (2021)
59. J.M. Arandes, I. Torre, M.J. Azkoiti, J. Erena, M. Olazar, J. Bilbao, *Energy Fuels.* **23**, 4215–4223 (2009)
60. K. Urata, S. Furukawa, T. Komatsu, *Appl. Catal. -Gen.* **475**, 335–340 (2014)
61. J.P. Ruelas-Leyva, L.F. Maldonado-Garcia, A. Talavera-Lopez, I.A. Santos-López, L.A. Picos-Corrales, C.E. Santolalla-Vargas, S.A.G. Torres, G.A. Fuentes, *Catalysts.* **11**, 128 (2021)

**Publisher's Note** Springer nature remains neutral with regard to jurisdictional claims in published maps and institutional affiliations.

Springer Nature or its licensor (e.g. a society or other partner) holds exclusive rights to this article under a publishing agreement with the author(s) or other rightsholder(s); author self-archiving of the accepted manuscript version of this article is solely governed by the terms of such publishing agreement and applicable law.